Inorganic Chemistry
Article
pubs.acs.org/IC

Synthesis and Characterization of Visible Light Absorbing $(GaN)_{1-x}(ZnO)_x$ Semiconductor Nanorods

Alexandra A. Reinert,[†] Candace Payne,[†] Limin Wang,[‡,⊥] James Ciston,[§,⊗] Yimei Zhu,[∥] and Peter G. Khalifah*[,†,‡]

[†]Department of Chemistry, Stony Brook University, Stony Brook, New York 11794, United States

[‡]Department of Chemistry, [§]Center for Functional Nanomaterials, and [∥]CMPMSD, Brookhaven National Laboratories, Upton, New York 11973, United States

Supporting Information

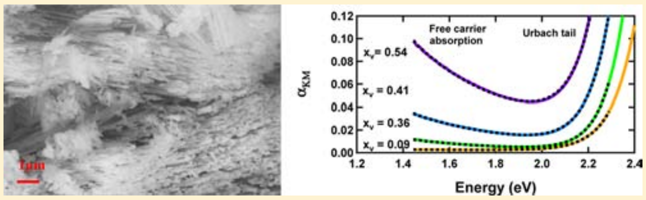

ABSTRACT: Although the $(GaN)_{1-x}(ZnO)_x$ solid solution is one of the most effective systems for driving overall solar water splitting with visible light, its quantum yield for overall water splitting using visible light photons has not yet reached ten percent. Understanding and controlling the nanoscale morphology of this system may allow its overall conversion efficiency to be raised to technologically relevant levels. We describe the use a $Ga_2O_3(ZnO)_{16}$ precursor phase in the synthesis of this phase which naturally results in the production of arrays of nanorods with favorable diameters (~100 nm) and band gaps (~2.5 eV). Substantial absorption within the band gap is observed, part of which is found to follow the E^{-3} scaling characteristic of free carriers scattered by ionized impurity sites. Compositional analysis suggests that a substantial quantity of cation vacancies (~3%) may be present in some samples. The typical nanorod growth direction and dominant $\{10\bar{1}1\}$ facet for powders in this system have been identified through electron microscopy methods, leading to the conclusion that polarity may play an important role in the high photoactivity of this family of wurtzite semiconductors.

■ INTRODUCTION

Solar water splitting can be accomplished by using a semiconductor to absorb solar energy, producing energetic electrons and holes that split H_2O to produce H_2 fuel and O_2 gas in two separate half-reactions. This process provides a renewable, clean, storable, and transportable source of energy. A number of semiconductors such as TiO_2 and $SrTiO_3$ have been demonstrated to have the ability to split water under ultraviolet (UV) light irradiation.[1,2] However, less than 5% of the total solar energy that illuminates earth is in the form of UV photons. A huge efficiency advantage can be gained if a semiconductor is found that can efficiently utilize the visible photons that make up more than 45% of the energy of the terrestrial solar spectrum, and the search for an ideal semiconductor of this type has motivated many scientific studies.[3,4]

Although the use of the visible part of the solar spectrum is important for increasing the efficiency of semiconductors used for this application, there are very few stable semiconductors which can effectively harness visible light to drive overall water splitting in the absence of an external potential. While it is not hard to find oxide semiconductors with band gaps smaller than TiO_2, most visible light absorbing semiconductors lack the ability to drive one (or both) of the half reactions for overall water splitting. One of the most successful oxide semiconductors for overall water splitting is $RbPb_2Nb_3O_{10}$, though the band gap of this compound (2.9 eV) is not much smaller than that of TiO_2.[5] A more typical behavior is observed for WO_3 which can drive water oxidation to produce O_2, but not H^+ reduction to form H_2.[6] There are limited possibilities for designing oxides for overall water splitting because of the strong electronegativity of the O^{2-} anion, leading to typical O 2p valence band edge positions which are about 1.5 eV lower in absolute energy than are minimally needed to drive water oxidation. When this is combined with the 1.23 V thermodynamic potential for water splitting and the typical need of an overpotential of 0.3 V to drive water oxidation, most conventional oxide semiconductors will be unable to drive overall water splitting with a band gap of less than 3 eV, precluding the effective utilization of the visible portion of the solar spectrum.

In contrast, nitrogen is substantially less electronegative than oxygen (3.0 vs 3.5 for oxygen on the Pauling scale). This will result in raised valence band energies for nitride or oxynitride analogues of oxide semiconductors, allowing the potential for overall water splitting with visible light without compromising the good stability that oxide semiconductors often exhibit under harsh redox conditions (the semiconductor must be less readily oxidized than water). A number of promising nitride and oxynitride systems for water splitting applications have been discovered in recent years. Both Ta_3N_5 (E_g = 2.1 eV) and TaON (E_g = 2.5 eV) have been demonstrated to be capable of driving water oxidation with reasonable quantum efficiencies

Received: January 2, 2013
Published: July 5, 2013

dx.doi.org/10.1021/ic400011n | Inorg. Chem. 2013, 52, 8389−8398

and stability.[7] Another visible light absorbing oxynitride, $LaTiO_2N$ with E_g = 2.2 eV, has been demonstrated to be capable of separately driving both O_2 and H_2 production in appropriate sacrificial reagents though it has not yet been observed to have a measurable activity for overall water splitting.[8,9] The most promising semiconductor discovered to date for stably driving overall water splitting with visible light is wurtzite-type $(GaN)_{1-x}(ZnO)_x$, which after extensive optimization[10−14] has been measured to drive overall water splitting with a quantum efficiency up to 6% with visible light photons.[15] There is no known reason why this efficiency could not be further improved to reach the higher values demonstrated by UV-driven semiconductors (60+%),[14] and this work strives to better understand and control the structural and electronic properties of the $(GaN)_{1-x}(ZnO)_x$ solid solution to open avenues for further improving its quantum efficiency.

GaN (E_g = 3.4 eV) and ZnO (E_g = 3.2 eV) are both well-known wide band gap semiconductors that are essentially transparent to visible light. These compounds are most stable in the wurtzite form (space group $P6_3mc$, #186), and have very similar lattice parameters (ZnO: a = 3.249 c = 5.207; GaN: a = 3.189 c = 5.185) (Figure 1). It was previously reported that these two end members can be combined to form a solid solution with a general formula of $(GaN)_{1-x}(ZnO)_x$ that can effectively absorb visible light, and can use electrons and holes generated in this manner to drive overall water splitting. It has been speculated that the band gap of this system can be reduced to about 2.4 eV,[4] an assertion supported by the observation of absorption edges (i.e., linear extrapolation to estimate the wavelength at which the onset of light absorption occurs), and as low as 2.5 eV[16] for compositions which have been measured to exhibit overall water splitting. Density functional theory (DFT) calculations on a variety of quasi-random structures have suggested that the band gap of this system can be reduced to 2.29 eV at a Zn content of x = 0.525.[17,18] More recent DFT work based on Monte Carlo simulations is supportive of this conclusion.[19]

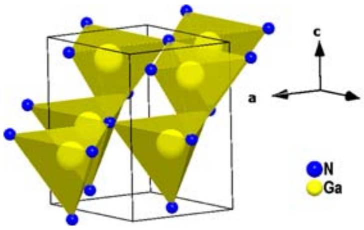

Figure 1. Wurtzite structure of GaN. All GaN_4 tetrahedra have the same orientation relative to the hexagonally close packed anion layers (apical oxygen points in −c direction), reflecting the polar nature of this structure.

A number of attempts have been made to improve the photoactivity of $(GaN)_{1-x}(ZnO)_x$ compounds by varying the synthetic method. It is clear that relatively high Zn contents are necessary to achieve the lowest band gaps in the $(GaN)_{1-x}(ZnO)_x$ system, but it has proven very challenging to experimentally achieve high x values because of the volatility of Zn under typical reaction conditions, which are highly reducing. The most Zn-rich samples prepared from binary oxides had a Zn content of x = 0.42.[20] High pressure synthesis was shown to be successful in producing $(GaN)_{1-x}(ZnO)_x$ with x = 0.50 and 0.75.[21] However, the restricted volume in high pressure syntheses has severely limited sample sizes and degree to which reaction products could be characterized. More recently, solution methods have been utilized to prepare a Ga−Zn−O layered double hydroxide route that can be used as a precursor to produce Zn-rich samples with x values of about 0.5−0.8, and band gaps that decreased from 2.6 to 2.35 eV with increasing Zn content.[22] These appeared to form porous particles without well-defined facets that maintained the overall shape of the precursor crystallites. This is consistent with prior work which determined that in reactions between Ga_2O_3 and ZnO, the particle size of the product depends most closely on the particle size of the ZnO reactant.[23] The use of nanoscale $ZnGa_2O_4$ and ZnO precursors has also produced Zn-rich samples with x values of about 0.30−0.87, and band gaps that decreased from 2.7 to 2.2 eV. This route produced single-crystalline particles with the use of a lower nitridation temperature (650 °C) than used in bulk syntheses (850 °C).[24] In other studies, it was observed that the spinel compound $ZnGa_2O_4$ makes a very effective precursor for the synthesis of $(GaN)_{1-x}(ZnO)_x$ because of the premixing of Ga and Zn on an atomic scale.[25,26] In this work, we have explored the use of alternative Ga−Zn−O precursors which are substantially more Zn-rich than $ZnGa_2O_4$. In particular, the m = 16 member of the $Ga_2O_3(ZnO)_m$ homologous series has been found to enable the synthesis of well-crystallized $(GaN)_{1-x}(ZnO)_x$ nanorods with high Zn contents and band gaps that are small relative to compounds prepared simply using a $ZnGa_2O_4$ spinel precursor.

There are a number of closely related homologous series with generic formulas of $A_2O_3(BO)_m$, where A = In, Fe, Ga and B = Fe, Zn,[27,28] among which the $In_2O_3(ZnO)_m$ compounds have been shown to be effective photocatalysts.[27] In $Ga_2O_3(ZnO)_m$,[29] variable width $(ZnO)_m$ layers form a block that closely approximates the wurtzite structure of ZnO,[30] as can be seen in Figure 2 for the structure of the m = 6 member,[29] the only compounds whose full structure has been solved. This makes them candidates for a facile, rapid, and potentially even topotactic transformation to wurtzite-type $(GaN)_{1-x}(ZnO)_x$ via high temperature treatment with ammonia. However, the crystallography of these phases is quite complex. The specific values of m which have been observed to form discrete phases are 6, 7, 8, 9, and 16. Extremely large unit cells have been reported on the basis of

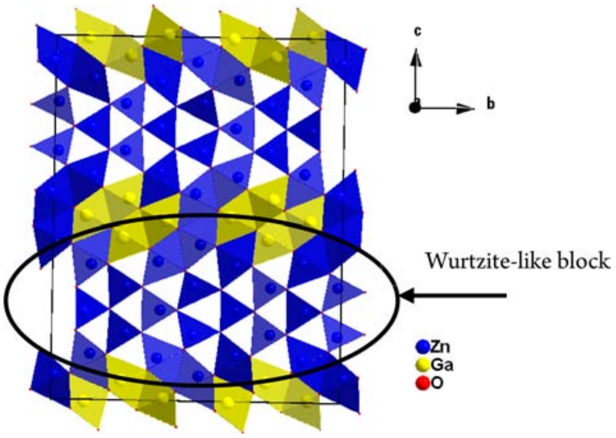

Figure 2. Orthorhombic structure of $Ga_2O_3(ZnO)_6$. Bond valence sum calculations using previously determined atomic positions[29] were used to assign crystallographic sites to either Ga or Zn.

prior single crystal diffraction studies, and the diffraction patterns that result from the various stacking variants are all quite similar to each other and to the parent wurtzite phase ($m = \infty$) because of their close structural relationship. It has been suggested that the symmetry of these compounds can most appropriately be described with a commensurately modulated superspace group.[29] Prior syntheses of these compounds were accomplished using platinum crucibles and very high temperatures at which Zn is easily volatilized and lost, and improvements on these synthetic procedures are necessary before the $Ga_2O_3(ZnO)_m$ phases can be effectively used as a precursor for the synthesis of bulk quantities of $(GaN)_{1-x}(ZnO)_x$.

■ EXPERIMENTAL SECTION

Synthesis. $Ga_2O_3(ZnO)_m$ phases were carried out by mixing stoichiometric amounts of Ga_2O_3 (Alfa Aesar, 99.999%) and ZnO (Alfa Aesar, 99.99%), grinding with an agate mortar and pestle, and placing the mixture in a dense alumina crucible (CoorsTek). The $m = 16$ phase used as a precursor for $(GaN)_{1-x}(ZnO)_x$ syntheses was obtained by reacting stoichiometric amounts of Ga_2O_3 and ZnO (1:16) in a sealed alumina tube held at 1350 °C (1623 K) under flowing oxygen (~60 mL/min) for a total of 144 h with intermediate grinding steps every 48 h to promote reactivity and product homogeneity. Conversion of the $Ga_2O_3(ZnO)_{16}$ precursor into a wurtize oxynitride was typically done at 1123 K under NH_3 flow (5 mL/min) for times of 10−18 h, resulting in single phase wurtzite samples with varying zinc contents. After heating, the sample was cooled to room temperature under NH_3 flow, and the tube was then purged with N_2 gas prior to sample removal.

X-ray Powder Diffraction. Progression of reactions was monitored using X-ray powder diffraction on a Bruker D8 Advance laboratory diffractometer (Cu K_α $\lambda = 1.54059$ Å, 7−120° 2θ, 0.02° step size, 300 mm radius, 12 mm variable slits (or 0.3° fixed divergence slits for Rietveld refinements), 2.5° Soller slits and a 192-channel Lynx-Eye 1D position sensitive Si detector). Scans for phase identification were collected with a scan rate of 0.1 s/step (19.2 s/point) while Rietveld scans were collected using a scan rate of 3 s/step (576 s/point). Zero background silicon slides were used as sample holders. The JADE software package (Materials Data, Inc.) was used for preliminary unit cell refinements and for phase identification. Rietveld refinements were carried using TOPAS v4.2 (Bruker AXS).

Scanning Electron Microscopy. Sample morphology and size were determined by scanning electron microscopy (SEM, LEO Gemini 1550, RBSD). Powder samples were mounted on circular aluminum standard sample studs using double sided carbon conductive tape. Images were taken at magnifications ranging from 300× to 100,000× using a 20 kV accelerating voltage and a working distance of 10 mm.

Diffuse Reflectance Spectroscopy. Optical properties of samples were measured using ultraviolet−visible diffuse reflectance spectroscopy (UV−vis DRS; PerkinElmer Lambda950). Powder samples were loaded into a cylindrical powder holder with a circular quartz window 16.60 mm in diameter and 1.50 mm thick. A scan range of 200−1000 nm (6.20−1.24 eV with a detector change at 860.80 nm and a lamp change at 319.20 nm) was used with a data interval of 1.30 nm and a scan rate of 182.25 nm/min and a $BaSO_4$ (Alfa Aesar, 99.998%) 100% reflectance standard.

Thermogravimetric Analysis. Thermogravimetric Analysis (TGA; Q500 or Q5000 system from TA Instruments) was used to determine the nitrogen content in samples. Alumina sample pans (100 μL) were used for powder sample masses of 10−20 mg, which were heated under a constant flow of O_2 (25 mL/min) and held at room temperature for at least 1 h before ramping in temperature to allow for gas flow stabilization. A constant ramp rate of 5 °C/min was used with holds at both 250 °C (4 h) and 950 °C (6 h). Mass loss determinations were made by comparing masses at 250 °C upon heating and cooling, allowing buoyancy errors to be avoided.

Transmission Electron Microscopy. Transmission electron microscopy experiments were performed in an FEI Titan 80−300 microscope equipped with a CEOS third order image aberration corrector and dedicated environmental gas cell. All high-resolution images were collected with a residual spherical aberration value of −2 μm, and recorded on a Gatan Ultrascan 1000 CCD detector. Tomographic data were collected in STEM mode with a probe convergence semiangle of 9 mrad and a detector collection range of 35−65 mrad. The differential pumping apertures of the environmental cell prevented collection angles of greater than 65 mrad. Tomography data was collected in 1 deg steps from −65 to +65 deg. Three-dimensional images were reconstructed using the FEI Inspect3D software using the simultaneous iterative reconstruction technique (SIRT) algorithm.

■ RESULTS AND DISCUSSION

Synthesis of $Ga_2O_3(ZnO)_m$ Precursor Phases. Although the potential utility of $Ga_2O_3(ZnO)_m$ to the synthesis of Zn-rich $(GaN)_{1-x}(ZnO)_x$ semiconductors is clear, prior literature synthesis routes for these layered wurtzite-related phases had the major disadvantage of requiring very high temperatures (1350−1650 °C) with Pt crucibles.[31] The high synthesis temperatures are particularly problematic as they can strongly promote the reduction of ZnO to Zn metal and the resulting rapid evaporation of Zn metal. Reactions to produce $Ga_2O_3(ZnO)_m$ were therefore carried out under flowing oxygen, which was effective in limiting the loss of Zn. The use of large sample masses (typically 20 g) and mostly filled cylindrical crucibles minimized the surface area to volume ratio and allowed the net mass loss due to evaporation over the course of the reaction to be limited to about 0.2%. The Ga−Zn−O phase diagram was explored in a coarse fashion to enable the minimal synthesis temperatures for various $Ga_2O_3(ZnO)_m$ to be identified and an approximate phase diagram to be constructed. Figure 3 shows that the only ternary phase stable at modest temperatures (<1200 °C) is the $ZnGa_2O_4$ spinel, and that the layered $Ga_2O_3(ZnO)_m$ phases first are observed at temperatures of 1300 °C or higher. The $m = 16$ layered phase with the largest wurtzite blocks is the only layered compound observed at 1300 °C, and successively higher temperatures are required to produce phases with smaller wurtzite blocks.

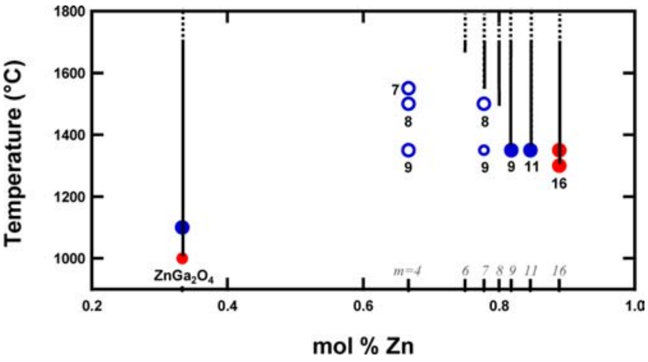

Figure 3. ZnO-Ga_2O_3 partial phase diagram. Closed circles represent single phase products and open circles represent multiphase samples containing $ZnGa_2O_4$ and a layered phase whose m value is indicated. No symbol is shown for the $m = 6$ phase which was prepared as a single crystal at 1650 °C without information about secondary phases. Red symbols denote samples synthesized in this work while blue symbols represent data from Kimizuka et al.[28,31] or Phani et al.[32].

At 1300 °C, reaction times of a week or longer are typically required to obtain a homogeneous product. The X-ray diffraction pattern of a typical reaction product is shown in Figure 4, with marked peak positions expected for the literature orthorhombic unit cell (a = 3.25, b = 19.76, c = 54.21 Å). It should be noted that X-ray diffraction patterns could not confirm that the $Ga_2O_3(ZnO)_{16}$ samples were single phase since the crystal structure has not yet been solved and refined. The pattern analysis is made more challenging since the $m = 16$ pattern inherently has a tremendous degree of peak overlap because of its large unit cell, has great similarity between the periodicities along different axes because of its close relationship with the wurtzite subcell, has a very large degree of peak overlap with other $Ga_2O_3(ZnO)_m$ phases, and has a structure which is likely conducive to the formation of stacking faults. It also appears that these phases are best described in terms of modulated structures that require more than three dimensions to be accurately indexed. As a result, reactions were judged to be complete when X-ray patterns no longer showed any evidence of starting materials or the spinel phase. The ability to synthesize $Ga_2O_3(ZnO)_m$ phases at temperatures lower than previously reported allowed the reactions to be carried out in alumina crucibles rather than in the more expensive Pt vessels used previously.

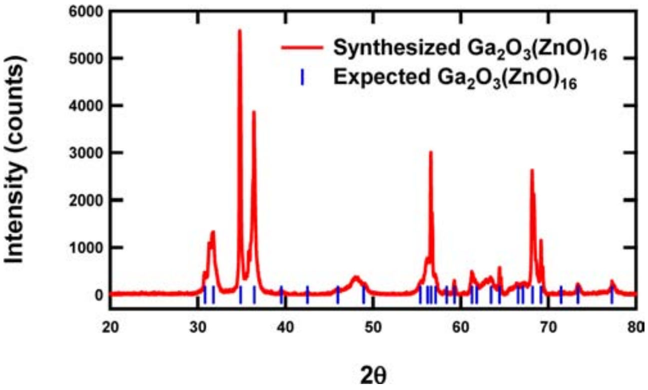

Figure 4. Powder XRD pattern of fully reacted $Ga_2O_3(ZnO)_{16}$. Selected peak positions expected for the literature unit cell without considering systematic absences are marked below the pattern.

The production of $(GaN)_{1-x}(ZnO)_x$ is typically accomplished by nitridation (high temperature treatment under flowing NH_3 gas) of precursors.[33] While this wurtzite phase was originally produced by the nitridation of Ga_2O_3 and ZnO mixtures,[33] it was later understood that these (and related precursors) typically quickly react to form the spinel compound $ZnGa_2O_4$, which then converts to wurtzite $(GaN)_{1-x}(ZnO)_x$ over a longer time scale.[21,25] It was later found that the nitridation of a $ZnGa_2O_4$ precursor will lead to products with very good photoactivity, perhaps facilitated because this compound has Ga and Zn homogenously mixed on an atomic scale. The spinel composition can at most lead to $ZnGa_2O_4$ with a cation mole fraction of Zn of $x = 0.33$, though the actual Zn content obtained in experiments was found to typically correspond to x values of 0.05–0.22[21,13] because of the facile loss of Zn through the mechanism of reduction to its metallic form followed by evaporation.

The use of a $Ga_2O_3(ZnO)_{16}$ precursor in nitridation reactions offers the same advantage of premixed Ga and Zn atoms as the spinel phase, but offers the potential to produce $(GaN)_{1-x}(ZnO)_x$ products which are Zn-rich and are therefore likely to have reduced band gaps and potentially better photoactivity for water splitting. The cation mole fraction of Zn is $x = 0.89$ for the $m = 16$ layered compound, and remains large even for the $m = 6$ compound which has $x = 0.75$. Further control over the Zn content of $(GaN)_{1-x}(ZnO)_x$ produced by nitridation reactions using a $Ga_2O_3(ZnO)_{16}$ precursor can be achieved by varying the reaction time, temperature profile, NH_3 flow rate, or any other parameter which influences the amount of Zn evaporation. About 10 important variables that influence Zn content were identified in experiments. To achieve the best reaction reproducibility and the greatest reduction of parameter space, all reaction parameters except for the reaction time and NH_3 flow rate were kept constant to the furthest extent possible. Because of the facile loss of Zn from $(GaN)_{1-x}(ZnO)_x$ phases, it was never possible to reach chemical equilibrium at the nitridation reaction temperature of 850 °C. However, single phase products with wurtzite X-ray diffraction patterns could be achieved (Figure 5). The substantial variation in the $(GaN)_{1-x}(ZnO)_x$ lattice parameters indicated that products with a wide range of Zn contents could be produced, and that high Zn contents were accessed.

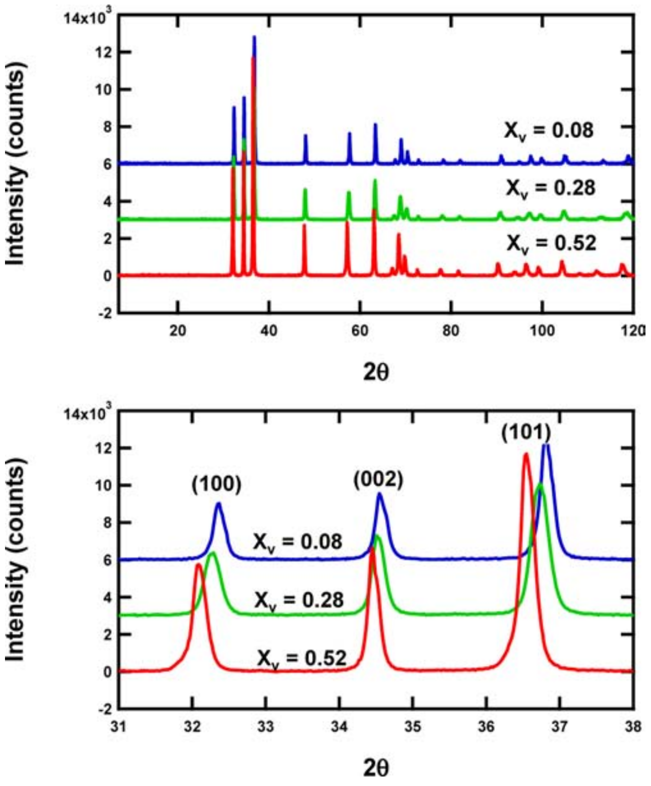

Figure 5. XRD patterns of $(GaN)_{1-x}(ZnO)_x$ produced from $Ga_2O_3(ZnO)_{16}$ precursor along with a zoomed image of prominent wurtzite peaks labeled with their Miller indices. Successive patterns are offset for clarity.

The accurate determination of the composition of $(GaN)_{1-x}(ZnO)_x$ wurtzite phases poses a significant challenge, especially when large numbers of samples are being screened. The use of energy dispersive X-ray spectroscopy (EDX) in a SEM microscope has been utilized in the past, but high accuracy with this technique is only achieved for flat samples (i.e., thin films, single crystals) and powder samples can routinely have errors in x of ±0.05 or worse. Furthermore, EDX will only be sensitive to Ga:Zn ratios as the light elements N and O cannot be accurately quantified by this method. In this study, a combination of TGA (to determine the N content) and quantitative phase analysis (QPA) by Rietveld refinement (to determine the Ga and Zn contents) were utilized to obtain accurate insights into $(GaN)_{1-x}(ZnO)_x$ stoichiometries in a manner which will be discussed more later. However, a more rapid compositional assessment that was used to provide precise and reproducible results was the Vegard's law analysis of the wurtzite *a*-lattice parameter. The relationship

$$a = 3.189 + 0.060x_v$$

was used to estimate a *nominal* Zn cation mole fraction, which will be denoted x_v, based on the assumption of a linear variation in the wurtzite *a*-lattice parameters between that of the end members of GaN ($x = 0$, $a = 3.189$) and ZnO ($x = 1$, $a = 3.249$). The high quality X-ray diffraction data allowed x_v to be determined with a precision of about 0.01. The accuracy of this method is not known absolutely, but based on analogies with other semiconductor systems it is expected that the *a*-lattice parameter increases monotonically with increasing Zn content and that an accuracy of about 0.05 will be achieved since there is no reason to expect strong bowing or other large deviations from Vegard's Law (linear change in lattice parameters with substitution) for the *a*-lattice parameter. As can be seen in Figure 5, there are about 20 discernible wurtzite X-ray diffraction peaks in a scan range of 7−120° 2θ, and that the peak shifts are large relative to the instrumental precision (~0.01° 2θ) even for the low angle peaks (30−40° 2θ) which are the least sensitive to lattice parameter changes, as can be seen in Figure 5.

Composition Determination. By following the mass changes that occur during oxidation, the nitrogen content of $(GaN)_{1-x}(ZnO)_x$ samples could be determined in TGA experiments (Figure 6). On heating, 1.5 atoms of O are needed to replace each N atom, giving rise to an expected mass gain of +11.93% when GaN is fully oxidized to Ga_2O_3, and a proportionally smaller mass change for $(GaN)_{1-x}(ZnO)_x$ samples with $x > 0$. The oxidation of GaN samples produced a mass change of 11.67%, slightly lower than the expected value. This could potentially be due to kinetic limitations as the decomposition of GaN took a long time to complete (>12 h at 950 °C) and did not show a clear plateau at 950 °C, unlike Zn-containing $(GaN)_{1-x}(ZnO)_x$ samples which were universally observed to be fully decomposed by the time the temperature ramp up to 950 °C was complete. The $x_v = 0.08$ sample was calculated to have an anion content of 82 mol % nitrogen, and the balance was attributed to oxygen ($\chi_O = 18\%$), while the $x_v = 0.28$ and $x_v = 0.52$ samples were calculated to have $\chi_O = 30\%$ and 53% oxygen, respectively, as summarized in Table 1.

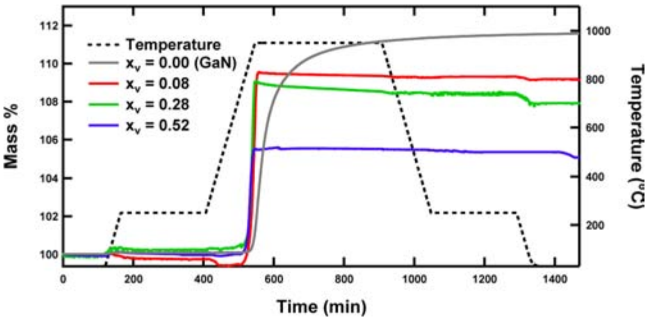

Figure 6. Mass changes observed during oxidation of $(GaN)_{1-x}(ZnO)_x$. GaN was synthesized by nitriding Ga metal.

Table 1. Compositional Analysis: Zn Content from Rietveld Refinements of TGA Products and O Content from TGA

	phase content from QPA (mass %)			ion fraction (mole %) by QPA(χ_{Zn}), TGA(χ_O)		
x_v	$ZnGa_2O_4$	Ga_2O_3	ZnO	χ_{Zn}	χ_O	R_{wp}
0.08	27.1(3)	72.9(3)		9	18	
0.28	68.1(2)	31.9(3)		23	30	6.52
0.52	71.1(1)		28.9(1)	54	53	

Further compositional information could be obtained by collecting X-ray diffraction patterns of the TGA decomposition products and carrying out quantitative phase analysis (QPA) by Rietveld refinement to determine the cation mole fraction of Zn and Ga. The TGA decomposition products that resulted from heating in flowing O_2 at 950 °C were a mixture of wurtzite ZnO, spinel $ZnGa_2O_4$, and monoclinic β-Ga_2O_3 in a manner generally consistent with the expected phase behavior of this system ($ZnGa_2O_4$ + β-Ga_2O_3 for samples with $x < 1/3$; $ZnGa_2O_4$ + ZnO for samples with $x > 1/3$). The Zn mole fraction (χ_{Zn}) was then determined from the ratio of products from the corresponding Rietveld refinements, reported in Table 1. This experimentally calculated Zn mole fraction was then compared to the Vegard's law approximation of Zn content (x_v) used to label samples.

The Zn contents of these samples determined from QPA are near the values estimated by x_v calculations (within 5 mol %). However, a more striking discrepancy can be seen in the oxygen contents of low Zn content samples which are indicative of a Zn:O ratio that is not equimolar. The origin of this nonstoichiometry is tentatively ascribed to wurtzite cation vacancies associated with Ga ions. In particular, it is known that treatment of Ga_2O_3 with NH_3 produces a very defective gallium oxynitride, whose formula has been reported as $Ga_{0.89}\square_{0.11}N_{0.66}O_{0.34}$,[34] while the ZnO lattice does not readily accommodate defects. Based on the experimentally determined Ga:Zn and N:O ratios, charge neutrality would be achieved with 3% cation vacancies in the $x_v = 0.08$ and $x_v = 0.28$ nanorod samples. It appears that cation defects may be important to understanding and improving the performance of wurtzite $(GaN)_{1-x}(ZnO)_x$ semiconductors, and further studies on these defects are in progress.

Spectroscopic Investigation of Band Structure. It has previously been reported that an increase in zinc content results in improved visible light absorption for $(GaN)_{1-x}(ZnO)_x$ samples with modest Zn contents ($x \leq 0.42$),[33,35] and this trend has more recently been seen to extend to Zn-rich samples.[21,22] The optical properties of nanorod $(GaN)_{1-x}(ZnO)_x$ samples prepared using a $Ga_2O_3(ZnO)_{16}$ precursor were determined by diffuse reflectance studies (Figure 7). The relative absorbance (α_{KM}) obtained from a Kubelka−Munk transform of the reflectance data showed increasing visible light absorption with increasing Zn content ($x_v \leq 0.55$), and similar behavior was observed for the band gaps (E_g) calculated from quantitative fits to the functional form expected for direct band gap absorption (Table 2).

The UV−vis optical response of $(GaN)_{1-x}(ZnO)_x$ has three characteristic regions, as shown in a representative fit for the $x_v = 0.55$ sample (Figure 8). The absorbance above the band gap

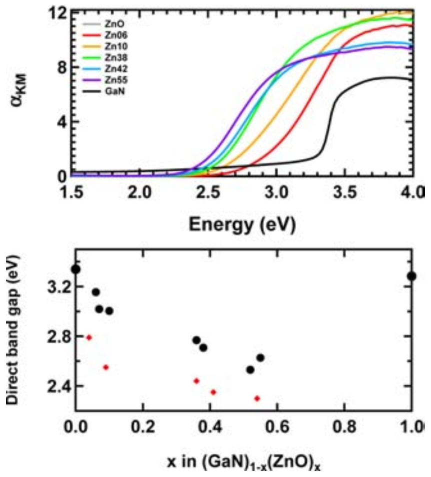

Figure 7. Top: Relative absorption spectra of $(GaN)_{1-x}(ZnO)_x$ samples with $x_v \leq 0.55$ obtained by nitriding a $Ga_2O_3(ZnO)_{16}$ precursor under a flow of NH_3 at 850 °C for varying times. Bottom: Direct band gap energy of $(GaN)_{1-x}(ZnO)_x$ as a function of x_v (large circles). Band edge energies are indicated with small diamonds.

Table 2. Optical Analysis: Values of Direct Band Edge and Urbach Tail Regions from Quantitative Fits to Functional Forms of Diffuse Reflectance Data

x_v	E_g from direct band gap fit	E_U from Urbach tail fit	E_g from Urbach tail fit	slope of free carrier region (B)
0.06	3.15	0.108	2.39	
0.10	3.00	0.090	2.41	0.001
0.38	2.77	0.083	2.50	0.037
0.42	2.71	0.090	2.49	0.102
0.55	2.53	0.094	2.43	0.286

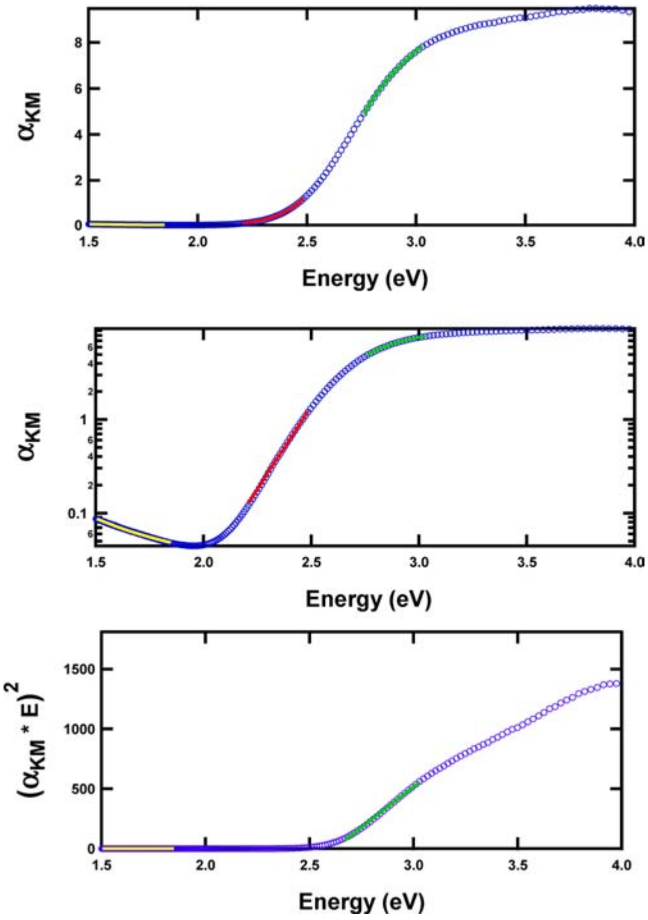

Figure 8. Optical response of $(GaN)_{1-x}(ZnO)_x$ x_v = 0.55 with the Kubelka−Munk-derived absorption scaled in three different manners to emphasize the regions where the absorbance is dominated by the direct band gap transitions (green line), the Urbach tail (red line), or free carrier absorption (yellow line).

of these wurtzite semiconductors was always characteristic of a direct band gap with $\alpha \sim (E - E_g)^{0.5}$, and an appropriate fitting range (green line) could be determined by looking for a linear region in a plot of $(\alpha E)^2$ vs E. However, this direct band gap scaling was only observed for regions of the spectrum where the absorbance was relatively large ($\alpha/\alpha_{max} > 0.5$) because of the presence of a very strong Urbach tail (red line), which resulted in substantial broadening of the onset of absorption and substantial absorption at sub-band gap energies. The Urbach-type absorption was fit using the functional form $\alpha = Ae^{(E - E_g)/E_U}$ where E_U is the Urbach energy that describes the breadth of the optical transition. This unusually large Urbach broadening was observed for all samples and is expected to reflect either compositional inhomogeneity (bulk or local) or the influence of a large concentration of defects.

Band gaps as low as 2.53 eV were observed for samples with the highest Zn contents, indicating that a substantial portion of the visible light spectrum can be absorbed by these nanorods. The optical data is generally consistent with those for samples prepared using other methods, though it should be noted that past literature has often used assessments of the band edge as a substitute for a proper band gap determination. The band edge is conventionally obtained by linearly extrapolating absorption to zero on a plot of α as a function of wavelength. Since this does not represent a proper functional form for light absorption, the band edge energy will necessarily differ from the band gap energy. For semiconductors like ZnO which have a sharp onset of absorption, this difference is typically small (<0.05 eV). Differences are exaggerated for semiconductors like $(GaN)_{1-x}(ZnO)_x$ which have a broad onset of absorption, and it was found that the band edge energies (small circles on Figure 7) determined for $(GaN)_{1-x}(ZnO)_x$ nanorods were commonly 0.25 eV smaller than their direct band gaps, suggesting that some prior estimates of $(GaN)_{1-x}(ZnO)_x$ band gaps need to be revised upward.

A third component of the optical absorption which has not been previously commented on for $(GaN)_{1-x}(ZnO)_x$ semiconductors is the absorption below the band gap which appears approximately linear when α is plotted on a log scale, and therefore substantially increases with decreasing energy (yellow line). We attribute this type of absorption to free carrier absorption, which is well-known to be strongest at low photon energies. It is hypothesized that Zn loss is a major mechanism for the introduction of carriers (previously reported to be holes)[36] into these wurtzite semiconductors, and that cation vacancies (or equivalently, excess anions) may be active in maintaining charge balance. This is consistent with the enhanced activity recently reported to result following the air annealing of $(GaN)_{1-x}(ZnO)_x$ with $x = 0.18$ at 550 °C.[37] The photoactivity of $(GaN)_{1-x}(ZnO)_x$ semiconductors is expected to strongly depend on their carrier concentration (which influences both band bending and the minority carrier diffusion length), and the below-gap optical absorption can potentially provide an easy and direct method for quantifying changes in the carrier concentration of powder samples introduced by physical processes or by chemical substitution.

In the simplest Drude model of free carriers, it is expected that free carrier absorption is proportional to λ^2, though other scaling relationships may be observed if other scattering processes are active, such as the $\lambda^{1.5}$ scaling when lattice vibrations are involved, or ionized impurity scattering which is expected to give either λ^3 or $\lambda^{3.5}$ scaling in different derivations.[38−40] Prior measurements on single crystal ZnO samples[41,42] have found λ^3 scaling that is robust over a range of free carrier and impurity concentrations, and have suggested the relationship $n_e = \alpha(E)\, E^3$ (2.24×10^{17} cm^{-2} eV^{-3}).[43] This relationship probably cannot be extrapolated to $(GaN)_{1-x}(ZnO)_x$ semiconductors since the proportionality constant relating n_e and $\alpha(E)$ will depend on the impurity concentration, which will be preparation-dependent and which is likely to be significantly different between binary ZnO and complex $(GaN)_{1-x}(ZnO)_x$. It has been shown for single crystal *n*-type germanium semiconductors[40] that absorption scales as either

$$\alpha(E) = n_e (m/m^*)^2 \lambda^2 f_e(T) \text{ for electronic-only scattering}$$

or

$$\alpha(E) = n_e N_i (m/m^*)^2 \lambda^3 f_i(T) \text{ for impurity scattering}$$

where n_e is the free carrier concentration, N_i is the concentration of ionized impurities, m and m^* are the actual and effective electron masses. The temperature dependence of absorption $f(T)$ is expected to scale as $\tau^2 T$ with the electron scattering lifetime τ for an electronic-only scattering mechanism, but is expected to be essentially independent of temperature when ionized impurities provide the dominant scattering mechanism.

Fits to the optical absorption of $(GaN)_{1-x}(ZnO)_x$ nanorods below the band gap to a combined Urbach and free carrier response (Figure 9, black dashed lines) with

$$\alpha(E) = A\cdot e^{(E-E_g)/E_U} + B\cdot E^{-3} + C$$

show that λ^3 (or equivalently, E^{-3}) scaling very accurately describes the energy dependence of their free carrier absorption, and that there is a very large difference in the absorption of samples with different substitution levels. It is clear that the free carrier absorption is much stronger in samples with high zinc contents, though it is not yet known if this is due to higher carrier concentrations or to higher levels of ionized impurities. Optimal performance for solar water splitting by $(GaN)_{1-x}(ZnO)_x$ nanorods can only be accomplished when both the impurity and carrier concentration are appropriate. Methods for deconvoluting their contributions to absorption that will enable their quantification by optical methods are the subject of ongoing work.

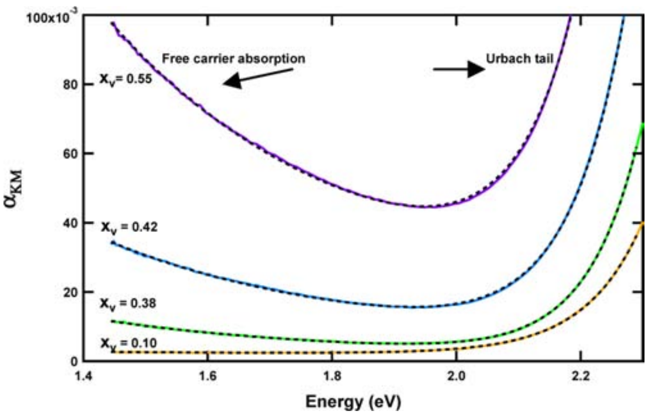

Figure 9. Below-band gap absorption of the $(GaN)_{1-x}(ZnO)_x$ relationship for samples with band gaps between 3.00 eV (x_v = 0.10) and 2.53 eV (x_v = 0.55) highlighting the free carrier absorption below 2.0 eV which increases substantially with increasing Zn content. Combined fits to an Urbach tail ($A\cdot e^{(E-E_g)/E_U}$), free carrier ($B\cdot E^{-3}$), and baseline offset (C) response are overlaid as dashed black lines for each sample.

Precursor Influence on Product Morphology. It has been previously demonstrated that both the nature of the precursor and the morphology of the precursor can strongly influence the morphology of wurtzite $(GaN)_{1-x}(ZnO)_x$ reaction products.[23] Initial insights were obtained from scanning electron microscopy experiments (Figure 10). Both $Ga_2O_3(ZnO)_{16}$ and $ZnGa_2O_4$ precursors were prepared using ZnO and β-Ga_2O_3 binary oxides which were dried in air at 700 °C for 2 h prior to use. The dried ZnO consisted of particles that were about 300 nm in diameter, while β-Ga_2O_3 has a rod-like morphology and a far larger particle size (rods up to 60 μm in length were visible). After these binary oxides were reacted in O_2 at 1350 °C to form $Ga_2O_3(ZnO)_{16}$ or in air at 1000 °C to form $ZnGa_2O_4$ precursors, polydisperse particles were observed. $Ga_2O_3(ZnO)_{16}$ consisted of agglomerates of particles with typical dimensions of 2 to 20 μm, while $ZnGa_2O_4$ spinel exhibited rod-like particles about 10 μm long.

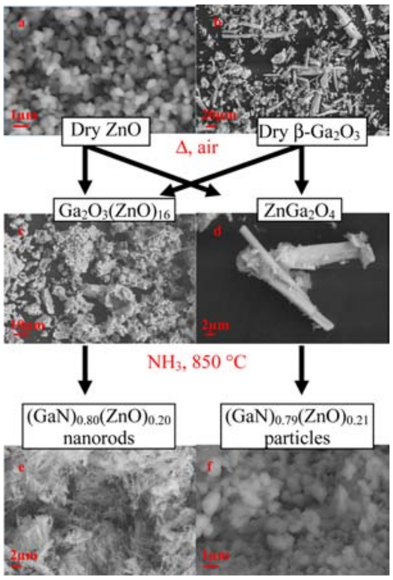

Figure 10. SEM images of (a) β-Ga_2O_3 dried at 700 °C, (b) ZnO dried at 700 °C, (c) $Ga_2O_3(ZnO)_{16}$ synthesized at 1350 °C, (d) $ZnGa_2O_4$ synthesized at 1000 °C, (e) $(GaN)_{1-x}(ZnO)_x$ from 2:16 synthesized at 850 °C with x_v = 0.20, (f) $(GaN)_{1-x}(ZnO)_x$ from $ZnGa_2O_4$ synthesized at 850 °C with x_v = 0.21.

Despite the comparable dimensions of the $Ga_2O_3(ZnO)_{16}$ and $ZnGa_2O_4$ precursors, the wurtzite reaction products obtained by ammonolysis at 850 °C had completely different morphologies. The cubic spinel precursor gave rise to roughly equiaxial particles about 0.5 μm in thickness, while the layered $Ga_2O_3(ZnO)_{16}$ precursor produced nanorods which were roughly 200 nm in diameter and 5 μm in length. Furthermore, these nanorods could be obtained in a carpet-like assembly with a high degree of alignment prior to dispersal, as seen in Figure 11. Two factors are believed to be responsible for promoting nanorod formation. First, the preexisting wurtzite-like layers in the $Ga_2O_3(ZnO)_{16}$ precursor are believed to serve as directing agents so that the large precursor particles convert in an equivalent manner across their breadth through a pathway that is not available to the highly symmetric cubic spinel phase. Second, a very substantial amount of Zn is lost via evaporation when the $Ga_2O_3(ZnO)_{16}$ precursor converts to wurtzite, and the space between the pillared nanorods represents an organization of the void spaces that result. The needle-like morphology is very desirable for water splitting applications as it permits short diffusion lengths for carriers to access the particle surface, while maintaining a large enough particle size to allow the development of band bending that can provide a driving force for charge separation between the photogenerated electrons and holes. Future comparative tests of the photoactivity of cocatalyst functionalized wurtzite nanorods to samples prepared by other methods will be used to determine if enhanced quantum yields for overall water splitting can be realized.

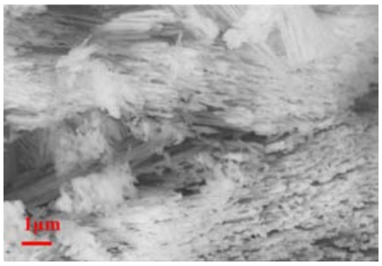

Figure 11. Nanorod "carpet" of $(GaN)_{1-x}(ZnO)_x$ with x_v = 0.33 resulting from the nitridation of $Ga_2O_3(ZnO)_{16}$ at 750 °C.

Further morphology studies were carried out using TEM techniques for $(GaN)_{1-x}(ZnO)_x$ samples synthesized from both $Ga_2O_3(ZnO)_{16}$ and $ZnGa_2O_4$ precursors with estimated compositions of x_v = 0.09, 0.21, and 0.54. Consistent with the SEM results, TEM reveals a rod-like morphology of most particles with lengths of 2−6 μm and 100−300 nm widths. It was confirmed by both transmission electron diffraction and high resolution imaging that the nonpolar $(12\bar{1}0)$ plane is perpendicular to the long axis of the rod, independent of the Ga/Zn ratio studied. Figure 12 shows a series of low resolution and high resolution images and electron diffraction pattern for the x_v = 0.21 $(GaN)_{1-x}(ZnO)_x$ prepared from a $Ga_2O_3(ZnO)_{16}$ precursor, which is representative of the rod morphology for all compositions studied. Extended annealing of the material for over 12 h resulted in particles of more isotropic shape because of high temperature coarsening, supporting the assertion that kinetic rather than thermodynamic driving forces were responsible for the initial nanorod morphology.

To determine the facet of $(GaN)_{1-x}(ZnO)_x$ that is active in solar photochemistry, TEM tomographic studies were carried out on samples prepared using the more common spinel precursor. In addition to being representative of samples whose activities have been studied in depth, the surface facets for spinel-derived samples are better defined than those of the novel nanorod samples. Tomographic tilt series were collected in medium angle annular dark field Scanning TEM (STEM) mode for three different $(GaN)_{1-x}(ZnO)_x$ particles with x_v = 0.21 synthesized from the spinel precursor, and electron diffraction patterns were recorded for selected high symmetry axes. Figure 13 shows a selected projection of one of these particles with an accompanying diffraction pattern to determine the facet identities. A tomographic reconstruction was used to distinguish facets viewed in profile from crystal edges viewed obliquely. Using a combination of three-dimensional tomographic reconstruction and cross-referenced diffraction data, a total of 22 surface facets from three particles were determined to be of the $\{10\underline{1}1\}$ plane group. This result is surprising because the $\{10\underline{1}1\}$ plane group represents a polar termination,

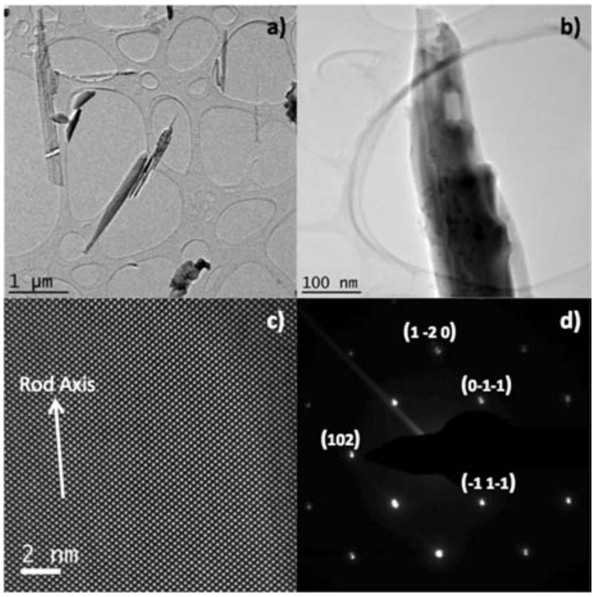

Figure 12. TEM images of x_v = 0.21 $(GaN)_{1-x}(ZnO)_x$ from 2:16 precursor (a) low resolution, (b) medium resolution, (c) high resolution, (d) electron diffraction indicating $(12\bar{1}0)$ rod growth plane.

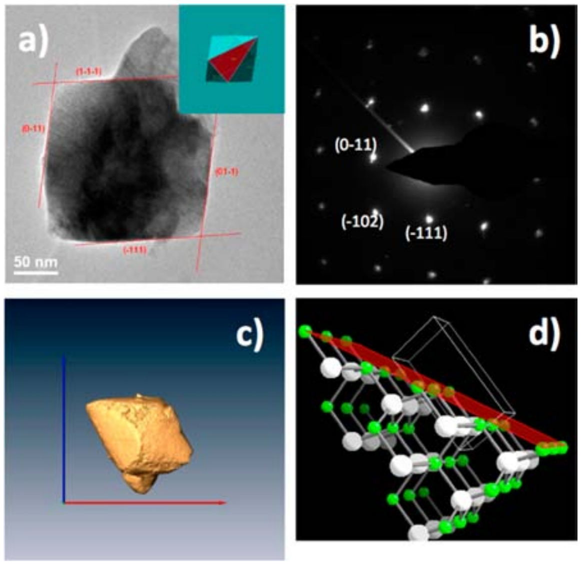

Figure 13. $(GaN)_{1-x}(ZnO)_x$ x_v = 0.21 from $ZnGa_2O_4$ precursor (a) TEM image, (b) electron diffraction pattern collected along [211] direction, (c) three-dimensional reconstruction of tomographic reconstruction, (d) atomic model of polar $\{10\bar{1}1\}$ termination.

which is expected to exhibit a high surface energy unless compensated by surface adsorbates, atomic reconstruction, or preferential termination of O or N planes to balance the excess valence.

The observation of potentially polar facets suggests that the superb photoactivity of $(GaN)_{1-x}(ZnO)_x$ wurtzite for overall water splitting may be facilitated by the polar space group ($P6_3/mmc$, #186) of this compound. The possible polarity of the $\{10\bar{1}1\}$ facets can be clearly seen in the alternating layers of cations and anions in the face normal direction (Figure 13d). Polarity may contribute to enhanced photoactivity of GZNO semiconductors in two manners. First, the polar GZNO surfaces may be substantially more reactive than nonpolar surfaces. It has been previously observed that MgO and NiO form low-energy metastable structures at polar {111} facets through spontaneous dissociative water adsorption.[44,45] It has also been observed experimentally[46] that water spontaneously dissociates on the polar GaN(0001) surfaces, a close chemical analogue of $(GaN)_{1-x}(ZnO)_x$. The dissociation of water is expected to be an initial step of the overall water splitting reaction, and as such, polar semiconductor surfaces may be advantageous for lowering the barrier for overall water splitting.

The second route for polarity to enhance the efficiency of semiconductor water splitting is through its internal field. This internal electrical field of a polar semiconductor will drive photogenerated electrons and holes in opposite directions, resulting in a physical separation of charges that should appreciably reduce the rate of charge recombination processes. Enhanced carrier lifetimes will directly increase the quantum efficiency of the semiconductor-driven photoelectrochemical reactions for water splitting. Charge separation driven by polarity is expected to retain its effectiveness in nanoparticles, unlike the charge separation driven by band-bending, a phenomenon which often requires semiconductor thicknesses on the order of one micrometer to fully develop. Internal semiconductor electric fields have been recently utilized to produce junction-free photovoltaics,[47] convincingly demonstrating that internal electric fields can strongly influence charge separation within semiconductors.

Interestingly, many of the best wide band gap semiconductors for driving overall water splitting are titanates, niobates, and tantalates that contain early transition metals whose tendency to displace away from the center of their normal octahedral coordination environment is commonly harnessed in ferroelectric materials such as $BaTiO_3$, indirectly suggesting that polarity may play a large but generally unrecognized role in promoting photoactivity. There have been experiments on $BaTiO_3/TiO_2$ composites which suggest a synergy occurs when the electric field of $BaTiO_3$ interacts with a surface coating of TiO_2.[48] Outside of these transition metals, single crystal photoelectrochemical studies on wurtzite ZnO have found quantum efficiencies for water oxidation of approximately 65%.[49] While the growth of nonpolar GaN films was a critical step in maximizing radiative carrier recombination to promote the efficient emission of blue light in LEDs,[50] the enhancement of polarity in $(GaN)_{1-x}(ZnO)_x$ semiconductors by methods such as producing particles with facets normal to the polar {0001} axis or by minimizing defects or surface reconstructions which suppress the development of an electrical dipole are suggested as promising pathways for inhibiting carrier recombination and substantially improving water splitting quantum yields in this system.

■ CONCLUSIONS

New synthesis methods have been developed for preparing a Zn-rich $Ga_2O_3(ZnO)_{16}$ compound belonging to the $Ga_2O_3(ZnO)_m$ homologous series whose structure contains layers closely related to the ZnO wurtzite structure. It is shown that $(GaN)_{1-x}(ZnO)_x$ nanorods with direct band gaps as low as 2.53 eV can be produced by the high temperature ammonia treatment of this precursor. Compositional analysis finds Zn contents up to $x \sim 0.55$ with evidence that Ga vacancies may be occurring at the 2−3% level for Ga-rich samples. TEM tomography studies conclusively show that the polar $\{10\bar{1}1\}$ facets are dominant in spinel-derived $(GaN)_{1-x}(ZnO)_x$, making this the active facet on which water splitting occurs. Polarity may play an important role in enhancing the charge separation and photoactivity of this phase, both by aiding charge separation (bulk polarity) and by enhancing surface reactivity with water (surface polarity).

■ ASSOCIATED CONTENT

Ⓢ Supporting Information

Additional low resolution and HRTEM images of $(GaN)_{1-x}(ZnO)_x$ samples synthesized are provided along with a video showing the tomographic tilt series used to construct facets in Figure 13 of this paper. Rietveld refinements, XRD patterns, and refined parameter values are also given for samples from QPA. This material is available free of charge via the Internet at http://pubs.acs.org.

■ AUTHOR INFORMATION

Corresponding Author

*E-mail: kpete@bnl.gov. Phone: (631)632-7996.

Present Addresses

⊥(L.W.) E-mail: Limin.Wang@ge.com. Phone: +86-21-38771985.
⊗(J.C.) E-mail: JCiston@lbl.gov. Phone: (510)495-8072

Author Contributions

Synthesis routes were developed by C.P. and A.R. All sample preparation and characterization was done by A.R. (with L.W. providing assistance in the determination of band gaps), with the exception of electron microscopy, which was performed by J.C. The research advisor of J.C. was Y.Z.; all other researchers were advised by P.K.

Notes

The authors declare no competing financial interest.

■ ACKNOWLEDGMENTS

This work was in part carried out at BNL under Contract DEAC02-98CH10886 with the U.S. Department of Energy. Funding was provided by the Department of Energy via a Hydrogen Fuel Initiative grant through the Solar Photochemistry program (P.K.); interactions with HFI collaborators E. Fujita, J. Muckerman, and J. Rodriguez are gratefully acknowledged. We also acknowledge M. Dawber and P. Allen at Stony Brook University for many insightful discussions on the physics of polar materials. Portions of this research were carried out at the Oak Ridge National Laboratory's Spallation Neutron Source sponsored by the Scientific User Facilities Division, Office of Basic Energy Sciences, U.S. Department of Energy. Optical data and electron microscopy data were collected at Brookhaven National Laboratory's Center for Functional Nanomaterials supported by the DOE under grant DE-AC02-98CH10886.

REFERENCES

(1) Wrighton, M. S.; Ellis, A. B.; Wolczanski, P. T.; Morse, D. L.; Abrahamson, H. B.; Ginley, D. S. *J. Am. Chem. Soc.* **1976**, *98* (10), 2774.
(2) Honda, K.; Fujishima, A. *Nature* **1972**, *238*, 37.
(3) Lewis, N. S.; Nocera, D. G. *Proc. Nat. Acad. Sci. U.S.A.* **2006**, *103*, 15729−15735.
(4) Domen, K.; Maeda, K. *Mater. Res. Bull.* **2011**, *36*, 25.
(5) Takata, T.; Tanaka, A.; Hara, M.; Kondo, J. N.; Domen, K. *Catal. Today* **1998**, *44* (1−4), 17.
(6) Osterloh, F. E. *Chem. Mater.* **2008**, *20*, 35.
(7) Hara, M.; Hitoki, G.; Takata, T.; Konda, J. N.; Kobayashi, H.; Domen, K. *Catal. Today* **2003**, *78*, 555.
(8) Kasahara, A.; Nukumizu, K.; Hitoki, G.; Takata, T.; Kondo, J. N.; Hara, M.; Kobayashi, H.; Domen, K. *J. Phys. Chem. A* **2002**, *106*, 6750.
(9) Kasahara, A.; Nukumizu, K.; Takata, T.; Kondo, J. N.; Hara, M.; Kobayashi, H.; Domen, K. *J. Phys. Chem. B* **2003**, *107*, 791.
(10) Maeda, K.; Domen, K. *J. Phys. Chem. C* **2007**, *111*, 7851.
(11) Hirai, T.; Maeda, K.; Yoshida, M.; Kubota, J.; Ikeda, S.; Matsumura, M.; Domen, K. *J. Phys. Chem. C* **2007**, *111*, 18853.
(12) Maeda, K.; Teramura, K.; Lu, D.; Saito, N.; Inoue, Y.; Domen, K. *J. Phys. Chem. C* **2007**, *111*, 7554.
(13) Maeda, K.; Teramura, K.; Takata, T.; Hara, M.; Saito, N.; Toda, K.; Inoue, Y.; Kobayashi, H.; Domen, K. *J. Phys. Chem. B* **2005**, *105*, 20504.
(14) Kudo, A.; Miseki, Y. *Chem. Soc. Rev.* **2009**, *38*, 253.
(15) Maeda, K.; Domen, K. *Chem. Mater. Rev.* **2010**, *22*, 612.
(16) Hashiguchi, H.; Maeda, K.; Abe, R.; Ishikawa, A.; Kubota, J.; Domen, K. *Bull. Chem. Soc. Jpn.* **2009**, *82* (3), 401.
(17) Jensen, L. L.; Muckerman, J. T.; Newton, M. D. *J. Phys. Chem. C.* **2008**, *112*, 3439.
(18) Wang, S.; Wang, L. *Phys. Rev. Lett.* **2010**, *104*, 065501.
(19) Li, L.; Muckerman; James, T.; Hybertsen; Mark, S.; Allen; Philip, B. *Phys. Rev. B* **2011**, *83*, 134202-1−134202-6.
(20) Maeda, K.; Teramura, K. *Nature* **2006**, *440*, 295.
(21) Chen, H. W., L.; Bai, J.; Hanson, J. C.; Warren, J. B.; Muckerman, J. T.; Fujita, E.; Rodriguez, J. A. *J. Phys. Chem. C* **2010**, *114*, 1809.
(22) Wang, J.; Huang, B.; Wang, Z.; Wang, P.; Cheng, H.; Zheng, Z.; Qin, X.; Zhang, X.; Dai, Y.; Whangbo, M. *J. Mater. Chem.* **2011**, *21*, 4562.
(23) Hisatomi, T.; Maeda, K.; Lu, D.; Domen, K. *ChemSusChem* **2009**, *2*, 336.
(24) Lee, K.; Tienes, B. M.; Wilker, M. B.; Schnitzenbaumer, K. J.; Dukovic, G. *Nano Lett.* **2012**, 12.
(25) Sun, X.; Maeda, K.; Le Faucheur, M.; Teramura, K.; Domen, K. *Appl. Catal., A* **2007**, *327*, 114.
(26) Chen, H. Y.; Wang, L. P.; Bai, J. M.; Hanson, J. C.; Warren, J. B.; Muckerman, J. T.; Fujita, E.; Rodriguez, J. A. *J. Phys. Chem. C* **2010**, *114* (4), 1809−1814.
(27) Michiue, Y.; Kimizuka, N. *Acta Crystallogr., Sect. B: Struct Sci.* **2009**, *B66*, 117.
(28) Kimizuka, N.; Isobe, M.; Nakamura, M. *J. Solid State Chem.* **1995**, *116*, 170.
(29) Michiue, Y.; Kimizuka, N.; Kanke, Y. *Acta Crystallogr., Sect. B: Struct. Sci.* **2008**, *64*, 521.
(30) Li, C.; Bando, Y.; Nakamura, M.; Kurashima, K.; Kimizuka, N. *Acta Crystallogr., Sect. B: Struct. Sci.* **1999**, *55*, 355.
(31) Kimizuka, N.; Isobe, M.; Nakamura, M.; Mohri, T. *J. Solid State Chem.* **1993**, *103*, 394.
(32) Phani, A. R.; Santucci, S.; Di Nardo, S.; Lozzi, L.; Passacantando, M.; Picozzi, P. *J. Mater. Sci.* **1998**, *33*, 3969.
(33) Maeda, K.; Takata, T.; Hara, M.; Saito, N.; Inoue, Y.; Kobayashi, H.; Domen, K. *J. Amer. Chem. Soc.* **2005**, *127*, 8286.
(34) Kikkawa, S.; Nagasaka, K.; Takeda, T.; Bailey, M.; Sakurai, T.; Miyamoto, Y. *J. Solid State Chem.* **2007**, 180.
(35) Maeda, K.; Teramura, K.; Saito, N.; Inoue, Y.; Kobayashi, H.; Domen, K. *Pure Appl. Chem.* **2006**, *78* (12), 2267.
(36) Han, W.; Zhang, Y.; Nam, C.; Black, C. T.; Mendez, E. E. *Appl. Phys. Lett.* **2010**, 97.
(37) Maeda, K.; Teramura, K.; Domen, K. *J. Catal.* **2008**, 254.
(38) Visvanathan, S. *Phys. Rev.* **1960**, *120* (2), 379.
(39) Fan, H. Y. *Rep. Prog. Phys.* **1956**, *19*, 107.
(40) Fan, H. Y.; Spitzer, W.; Collins, R. J. *Phys. Rev.* **1956**, *101* (2), 566.
(41) Thomas, D. G. *J. Phys. Chem. Solids* **1959**, *10*, 47.
(42) Weiher, R. L. *Phys. Rev.* **1966**, *152* (2), 736.
(43) Vanheusden, K.; Warren, W. L.; Seager, C. H.; Tallant, D. R.; Voigt, J. A. *J. Appl. Phys.* **1996**, *79*, 7983.
(44) Ciston, J.; Subramanian, A.; Marks, L. D. *Phys. Rev. B* **2009**, *79*, 085421.
(45) Ciston, J.; Subramanian, A.; Kienzle, D. M.; Marks, L. D. *Surf. Sci.* **2010**, *604*, 155−164.
(46) Bermudez, V. M.; Long, J. P. *Surf. Sci.* **2000**, 450.
(47) Choi, T.; Lee, S.; Choi, Y. J.; Kiryukhin, V.; Cheong, S. W. *Science* **2009**, *324* (5923), 63−66.
(48) Li, L.; Rohrer, G. S.; Salvador, P. A. *J. Am. Ceram. Soc.* **2012**, *95* (4), 1414−1420.
(49) Paulauskas, I. E.; Katz, J. E.; Jellison, G. E.; Lewis, N. S.; Boatner, L. A. *Thin Solid Films* **2008**, *516* (22), 8175−8178.
(50) Waltereit, P.; Brandt, O.; Trampert, A.; Grahn, H. T.; Menniger, J.; Ramsteiner, M.; Reiche, M.; Ploog, K. H. *Nature* **2000**, 406.